In vitro corrosion resistance of a Ta_2O_5 nanofilm on MAO coated magnesium alloy AZ31 by atomic layer deposition

Chang-Yang Li[a,1], Chi Yu[a,1], Rong-Chang Zeng[a,d,*], Bo-Cheng Zhang[b,**], Lan-Yue Cui[a], Jun Wan[b], Yang Xia[c]

[a] *Corrosion Laboratory for Light Metals, College of Materials Science and Engineering, Shandong University of Science and Technology, Qingdao, 266590, China*
[b] *Jiaxing Microelectronics Engineering Center, Chinese Academy of Sciences, Jiaxing, 314022, China*
[c] *Institute of Microelectronics, Chinese Academy of Sciences, Beijing, 100029, China*
[d] *School of Materials Science and Engineering, Zhengzhou University, Zhengzhou, 450002, China*

ARTICLE INFO

ABSTRACT

Micro-arc oxidation (MAO) coating with outstanding adhesion strength to Mg alloys has attracted more and more attention. However, owing to the porous structure, aggressive ions easily invaded the MAO/substrate interface through the through pores, limiting long-term corrosion resistance. Therefore, a dense and biocompatible tantalum oxide (Ta_2O_5) nanofilm was deposited on MAO coated Mg alloy AZ31 through atomic layer deposition (ALD) technique to seal the micropores and regulate the degradation rate. Surface micrography, chemical compositions and crystallographic structure were characterized using FE-SEM, EDS, XPS and XRD. The corrosion resistance of all samples was evaluated through electrochemical and hydrogen evolution tests. Results revealed that the Ta_2O_5 film mainly existed in the form of amorphousness. Moreover, uniform deposition of Ta_2O_5 film and effective sealing of micropores and microcracks in MAO coating were achieved. The current density (i_{corr}) of the composite coating decreased three orders of magnitude than that of the substrate and MAO coating, improving corrosion resistance. Besides, the formation and corrosion resistance mechanisms of the composite coating were proposed.

1. Introduction

Magnesium (Mg) and its alloys are a new generation of biodegradable implant materials with good biocompatibility and similar mechanical properties to human bones [1–4]. As a bone nail or plate, it will automatically degrade after satisfying a certain service period, preventing the injury of secondary surgery [5]. However, the excessively fast corrosion rate of Mg alloys limits its applications [6]. The α-Mg reacted with OH- produces hydrogen during the corrosion process, and the excessively fast corrosion rate causes gas to accumulate, leading to localized allergic reactions [7]. Therefore, it is urgent for the development of an effective anti-corrosion coating in the current scale application of Mg alloys.

At present, surface modification technologies, including micro-arc oxidation (MAO) [8–10], chemical conversion treatment [11–13], layer by layer [14,15], etc., have been applied to protect Mg alloys. MAO

treatment is one of the most effective surface technologies, which is applied to an electrochemical method to form a stable oxide film to improve the corrosion resistance of Mg alloys [16–18]. The oxide film is *in-situ* grown on the Mg alloy substrate and has excellent adhesion to the substrate [19].

Note that, MAO coated Mg alloy has many micropores and microcracks. Aggressive ions intrude the MAO/substrate interface through the through pores, resulting in galvanic corrosion [20]. Therefore, it is necessary to further provide protection by post-processing such as sealing. Furthermore, MAO coating sealed methods according to the principle mainly include hydration reaction [21], alkali treatment [22], inorganic [23,24] and organic filling materials [17,25].

The hydration reaction [21] and the alkali treatment [22] are to place the MAO coating in boiling water or an alkaline solution (*e.g.* NaOH) to form a hydroxide (*e.g.* $Mg(OH)_2$) and generate volume expansion, achieving the purpose of sealing. However, the above methods

are very limited. Because Mg(OH)₂ could also lose H₂O molecules into an oxide film in a dry environment and the pore size returned to its original size.

Inorganic material fillings (*e.g.* sol-gel) and organic material fillings (*e.g.* polylactic acid (PLA)) are used as sealers. As a physical sealing, the sol-gel coating inevitably generates microcracks during drying, resulting in the reduction of long-term corrosion resistance [23,24]. In addition, Zeng et al. [25] prepared a MAO/PLA composite coating on Mg–1Li–1Ca alloy, which showed that the effective life of MAO coatings in simulated body fluids was only over 50 h. After soaking for 140 h, the PLA coating exhibited a bubble-drop phenomenon. The main reason was that PLA had a high-water permeability, and was mechanically or physically combined with MAO coating, that is, the binding force was weak. Although these methods have a certain protective effect, the weak bonding force is easy cause organic coating to peel off. The hydrolysis of organic coatings also is a problem for long-term protection.

Atomic layer deposition (ALD) [26,27] with the features of self-limiting and self-saturating can achieve of film thickness on the order of monoatomic layers. And completely uniform and conformal film coverage is achieved on a three-dimensional structure with a large aspect ratio. Therefore, ALD technology can be effectively used to seal the surface micropores of the MAO coating. In addition, it has been reported that tantalum (Ta) is more corrosion resistant and biocompatible than the currently used stainless steel and titanium (Ti) alloys [28], especially porous Ta metal [29], and high porosity, suitable pore size and three-dimensional structural characteristics [30,31]. Wang et al. [29] fabricated porous Ta and Ti with the same parameters using the 3D printing technology, which found that they had similar mechanical capabilities to trabecular bone *in vitro* and *in vivo*, and had the same human bone marrow mesenchyme stem cells proliferation and differentiation ability as porous Ti, indicating good mechanical compatibility and biocompatibility. Xu et al. [32] prepared a β-Ta₂O₅ coating on the Ti–6Al–4V alloy. The results of *in vitro* cell culture revealed that the adhesion and proliferation of mouse embryonic fibroblast cells on the β-Ta₂O₅ coated substrate was better than that of the bare substrate, reflecting its excellent biocompatibility. And the good corrosion resistance and biocompatibility of Ta metal are closely related to the dense oxides of the outer layer, attracting more and more attention, especially in the field of orthopedics.

In this study, a dense tantalum oxide (Ta₂O₅) film was prepared on MAO coated Mg alloy AZ31 by the ALD technique to seal the micropores and improve corrosion resistance. The corrosion resistance of the composite coating was evaluated, and the formation and corrosion resistance mechanisms were proposed.

2. Experimental

2.1. Materials and specimen preparation

Mg alloy AZ31 with a size of 20 mm × 20 mm × 5 mm was as-extruded and supplied by the Shandong Yin Guang Yu Yuan Light Metal Precision Molding Co., Ltd., China, which included 2.5–3.0 wt% Al, 0.7–1.3 wt% Zn, Mn > 0.20 wt%, Si ≤ 0.3 wt%, Cu ≤ 0.05 wt%, Ni ≤ 0.005 wt%, Fe ≤ 0.005 wt% and balanced Mg. Prior to the preparation of the coating, the samples were ground to 1500 grit, rinsed in deionized water, degreased in ethanol and dried in warm air.

2.2. Preparation of MAO coating

The MAO treatment device consisted of a pure Ti plate served as the cathode, a power supply unit controlled by a single chip micyoco (SCM) and a stirring/cooling system [17]. MAO procedures were conducted in a phosphoric electrolyte, containing 8 g/L of phytic acid and 10 g/L of NaOH. The MAO coating was treated at a gradually increasing voltage from 0 to 250 V with a frequency of 100 Hz and the duty cycle of 50% oxidized for 5 min at room temperature.

2.3. Fabrication of MAO/Ta₂O₅ coating

Ta₂O₅ films were deposited on the MAO coated Mg alloy AZ31 through ALD using a KE-Micro T200A atomic layer deposition system where the Ta and O sources were tris(diethylamido)(tert-butylimido) tantalum ($C_{16}H_{39}N_4Ta$, CAS:169896-41-7) and H₂O, respectively. A cylindrical shaped reactor with a diameter of 200 mm was used. During the deposition process, Ta, H₂O sources and delivery lines were kept at 130, 20 and 150 °C, respectively. The Ta concentration was controlled by changing the frequency of the $C_{16}H_{39}N_4Ta$ precursor cycle. High-purity N₂ (99.999%) was used as the carrier and purging gas with a constant flow rate of 8 sccm (Standard Cubic Centimeter per Minute) throughout all cycles during the ALD process. One complete Ta₂O₅ ALD cycle was carried out through the gas filling of $C_{16}H_{39}N_4Ta$ and H₂O with 0.1 and 0.015 s pulse, respectively, followed by the purge of N₂ for 60 s to eliminate the oversupplied $C_{16}H_{39}N_4Ta$, H₂O and by-products, preventing chemical vapor deposition from occurring. The growth rate of Ta₂O₅ was about 0.1 nm per cycle, which was similar to formerly published results [33,34]. The entire ALD deposition process was performed for 500 cycles.

2.4. Surface analysis

A field-emission scanning electron microscopy (FE-SEM, Nova NanoSEM 450, USA) was employed to discern the surface morphologies of MAO and MAO/Ta₂O₅ coatings and chemical compositions of the coatings was detected through an energy dispersive X-ray spectrometry (EDS). Crystallographic structures of the substrate, MAO coating, and MAO/Ta₂O₅ coating were analyzed by an X-ray diffractometer (XRD, Rigaku D/MAX2500PC, Japan) with a Cu target (λ = 0.154 nm) at 8°/min scanning rate over 2θ range from 5 to 80°. And the corrosion morphologies after immersion in Hank's solution for 294 h were also observed using FE-SEM. Chemical compositions of MAO/Ta₂O₅ coating were further determined by X-ray photoelectron spectroscopy (XPS, ESCALab250, Thermo Scientific, US) with an Al Kα X-ray source.

2.5. Corrosion resistance evaluations

Potentiodynamic polarization (PDP) curves and electrochemical impedance spectroscopy (EIS) measurements were performed on an electrochemical workstation (PAR Model 2273, Princeton, USA) connected to a three-electrode cell with coated and uncoated samples as the working electrode with an exposed area of 1 cm², a saturated calomel electrode (SCE) as the reference electrode and a platinum electrode as the counter electrode. All electrochemical measurements were conducted in Hank's solution (8.0 g/L NaCl, 1.0 g/L $C_6H_6O_6$ (Glucose), 0.35 g/L NaHCO₃, 0.4 g/L KCl, 0.14 g/L CaCl₂, 0.1 g/L MgCl₂·6H₂O, 0.06 g/L MgSO₄·7H₂O, 0.06 g/L KH₂PO₄ and 0.06 g/L Na₂HPO₄·12H₂O) at room temperature. Potentiodynamic polarization curves were derived at a sweep rate of 1 mV/s from −2.0 to −0.8 V/SCE. In EIS measurements, the frequency ranged from 100 kHz to 10 mHz and the amplitude of the sinusoidal potential signal was 10 mV/SCE. The equivalent circuits of EIS were fitted with the ZSimpWin software.

Hydrogen evolution tests were measured to evaluate the corrosion behavior of the substrate and its coatings during immersion in Hank's solution at 37.5 ± 0.1 °C for 294 h. The ratio of the sample surface area to the medium volume was approximately 40 mL/cm². The method for the hydrogen evolution test was reported in our previous literature [17]. All tests were repeated in triplicate.

3. Results

3.1. Surface morphologies

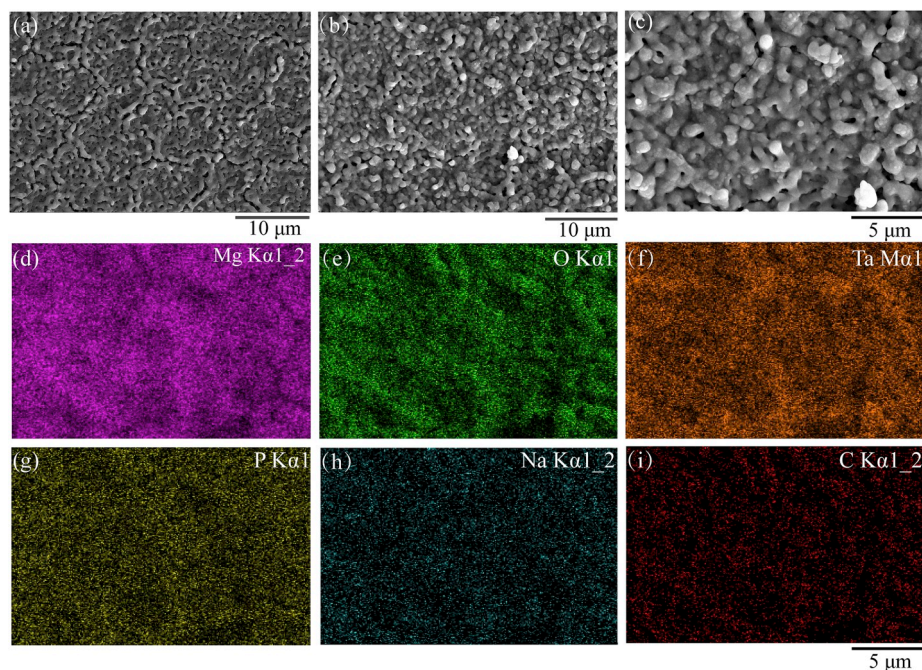Fig. 1 shows a comparison of SEM images of (a) MAO and (b, c)

Fig. 1. SEM images of (a) MAO and (b, c) MAO/Ta$_2$O$_5$ coatings; elemental mapping images of (d) Mg, (e) O, (f) Ta, (g) P, (h) Na, and (i) C for MAO/Ta$_2$O$_5$ coating.

MAO/Ta$_2$O$_5$ coatings. It could be seen that MAO coating (Fig. 1a) had typical microporous and microcrack structures, resulting from the generation of a large number of sparks and bubbles on the substrate under high-temperature and high-voltage conditions. After the Ta$_2$O$_5$ coating was prepared using ALD, the microcracks and microporous on the MAO coating surface were significantly reduced, and the convex portions were slightly enlarged in Fig. 1b and c. The MAO/Ta$_2$O$_5$ coating mainly contained Mg, O, Ta, P and trace Na and C elements (Fig. 1d–i). The distribution of Ta elements was very uniform. Mg elements were mainly derived from the substrate and MAO coating, O elements from MAO and Ta$_2$O$_5$ coatings and P element from the phytic acid in the electrolyte, indicating that the Ta$_2$O$_5$ was successfully and uniformly deposited on the surface of MAO samples. Furthermore, according to our previous reports [8,35], the thickness of the MAO coating was approximately 3 μm. Moreover, the deposition rate of Ta$_2$O$_5$ was 0.1 nm per cycle. Thence, the coating thickness of Ta$_2$O$_5$ after 500 cycles was about 50 nm.

Fig. 2 illustrates the XRD patterns of (a) the substrate, (b) MAO coating and (c) MAO/Ta$_2$O$_5$ coating. Obviously, the typical diffraction peaks of α-Mg including (100), (002), (101), (102), (110), (103), (200), (112), (201) and (004) were observed in all samples (JCPDS 65–3365). It can be seen that both MAO (Fig. 2b) and MAO/Ta$_2$O$_5$ (Fig. 2c) coatings contained the diffraction peaks of MgO including (200) and (220) (JCPDS 65–0476). And diffraction peaks intensity of MgO in the MAO/Ta$_2$O$_5$ coating was lower than that of the MAO coating. Strangely, no diffraction peaks of any Ta$_2$O$_5$ were detected, which could be ascribed that Ta$_2$O$_5$ existed in the form of amorphousness. In addition, the diffraction peaks of MgO in MAO/Ta$_2$O$_5$ coating were weakened, which might be resulted from the cover of the outer Ta$_2$O$_5$ coating. These can be confirmed by the EDS analysis in Fig. 1 and the next XPS analysis in Fig. 3.

XPS was performed to understand the composition and chemical bonding of the surface of MAO/Ta$_2$O$_5$ coating. Fig. 3 displays that XPS survey scan of (a) MAO/Ta$_2$O$_5$ coating, and high resolutions of the (b) Ta 4d, (c) Ta 4f and O 2s, (d) O 1s, (e) N 1s and (f) C 1s peaks. All data were calibrated by standard spectrogram C 1s at 284.6 eV. It could be seen that MAO/Ta$_2$O$_5$ coating surface mainly contained C, O, N and Ta elements. Especially, the spectrum of Ta 4d (Fig. 3b) was divided into Ta$_2$O$_5$ with continuous double peaks at 241.31 eV and 229.65 eV [36]
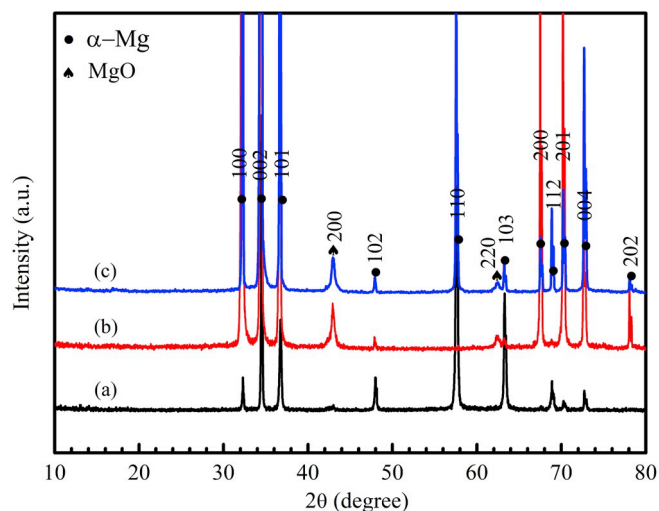

Fig. 2. XRD patterns of (a) substrate, (b) MAO coating and (c) MAO/Ta$_2$O$_5$ coating.

and the spectrum of Ta 4f and O 2s (Fig. 3c) were decomposed into multiple peaks, corresponding to Ta$_2$O$_5$ (27.28 eV and 25.36 eV) [37,38] and N–Ta (21.07 eV) [39,40]. Moreover, the peak of N–Ta indicated that the precursor source of C$_{16}$H$_{39}$N$_4$Ta did not completely react with H$_2$O during the ALD deposition process. The spectrum of O 1s (Fig. 3d) corresponded to Ta–O (530.63 eV) [41], further confirming the existence of Ta$_2$O$_5$. The spectrum of N 1s (Fig. 3e) was differentiated into N–C at 404.43 eV and N–Ta at 401.04 eV, which also indicated that the Ta source was not completely oxidized. The spectrum of C 1s (Fig. 3f) consisted of C–C at 284.60 eV and N–C at 283.00 eV, which agreed with the results of the N 1s peak, and also proved the residue of Ta source. In summary, the Ta$_2$O$_5$ coating was successfully prepared through ALD.

3.2. Electrochemical tests

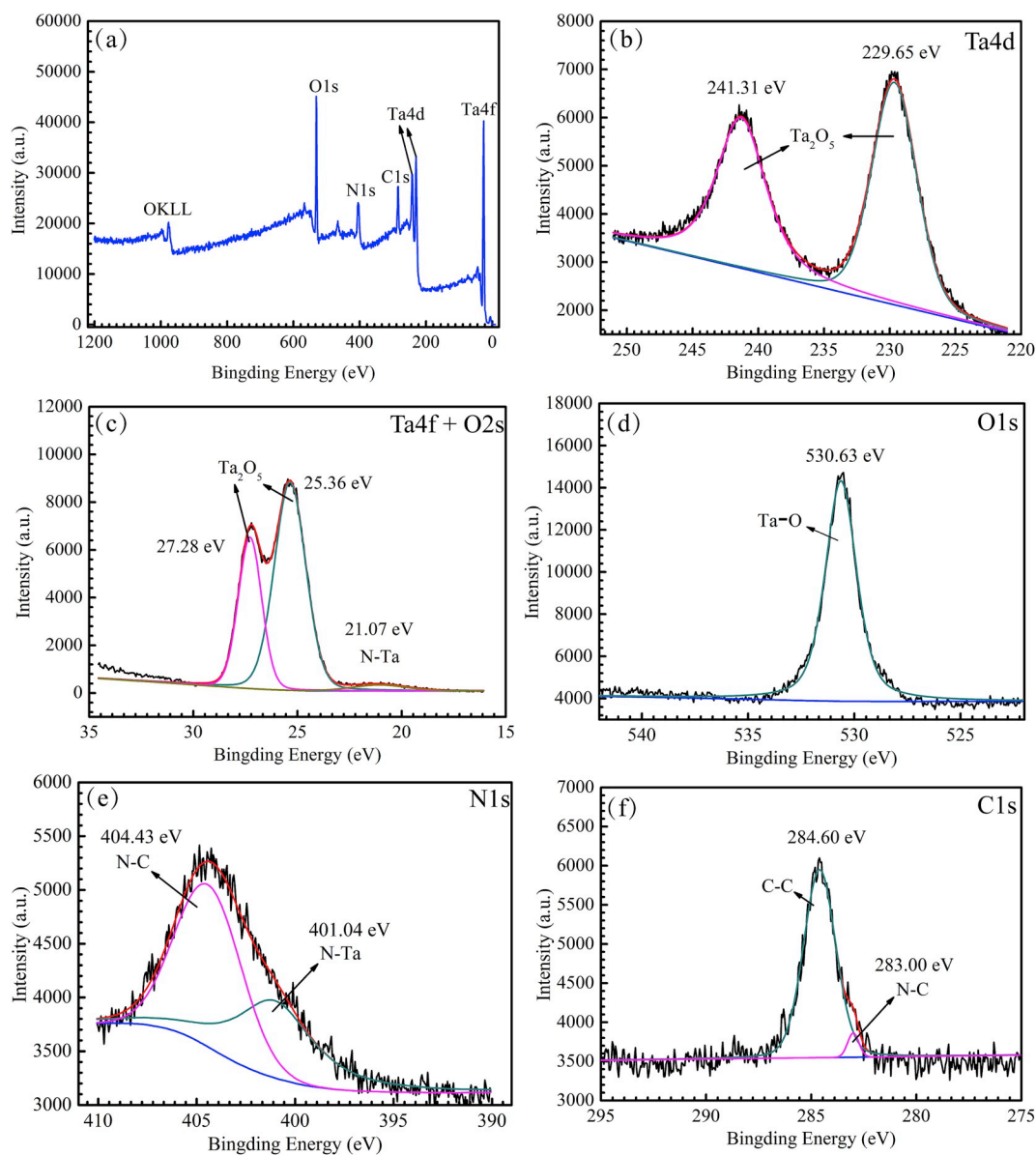Fig. 4 demonstrates that the PDP curves of (a) substrate, (b) MAO

Fig. 3. XPS survey scan of (a) MAO/Ta$_2$O$_5$ coating and high resolutions of the (b) Ta 4d, (c) Ta 4f and O 2s, (d) O 1s, (e) N 1s and (f) C 1s peaks.
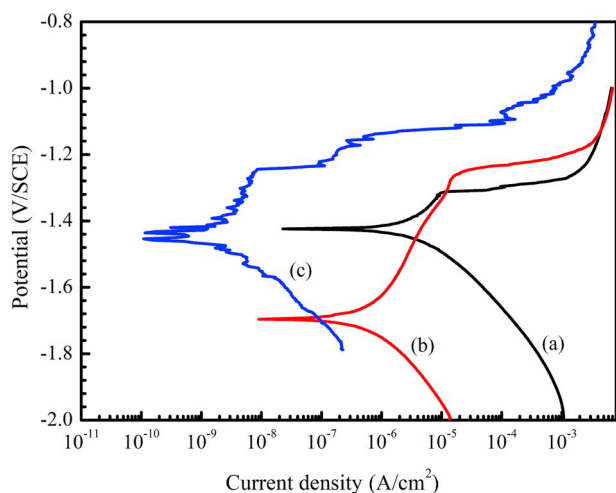

Fig. 4. PDP curves of (a) substrate, (b) MAO coating and (c) MAO/Ta$_2$O$_5$ coating in Hank's solution.

Table 1
Comparison of E_{corr} and i_{corr} with different treatment processes.

Samples	E_{corr} (V/SCE)	i_{corr} (A/cm^2)
substrate	−1.42	5.88×10^{-6}
MAO coating	−1.70	1.05×10^{-6}
MAO/Ta$_2$O$_5$ coating	−1.44	2.23×10^{-9}

coating and (c) MAO/Ta$_2$O$_5$ coating in Hank's solution. The relevant electrochemical parameters are counted in Table 1. It could be seen that the corrosion current density (i_{corr}) of the coated samples was smaller than that of the substrate, which could be ranged in increasing order: MAO/Ta$_2$O$_5$ coating < MAO coating < the substrate. Furthermore, the i_{corr} of MAO/Ta$_2$O$_5$ coating decreased three orders of magnitude than that of the MAO coating, from 1.05×10^{-6} A/cm^2 to 2.23×10^{-9} A/cm^2. This might be because Ta$_2$O$_5$ layer prepared through ALD blocked the micropores and microcracks in MAO coating, effectively improving corrosion resistance. The corrosion potential (E_{corr}) decreased from −1.42 V/SCE for the substrate to −1.70 V/SCE for MAO coating, indicating the presence of micro-galvanic effect [20]. And the
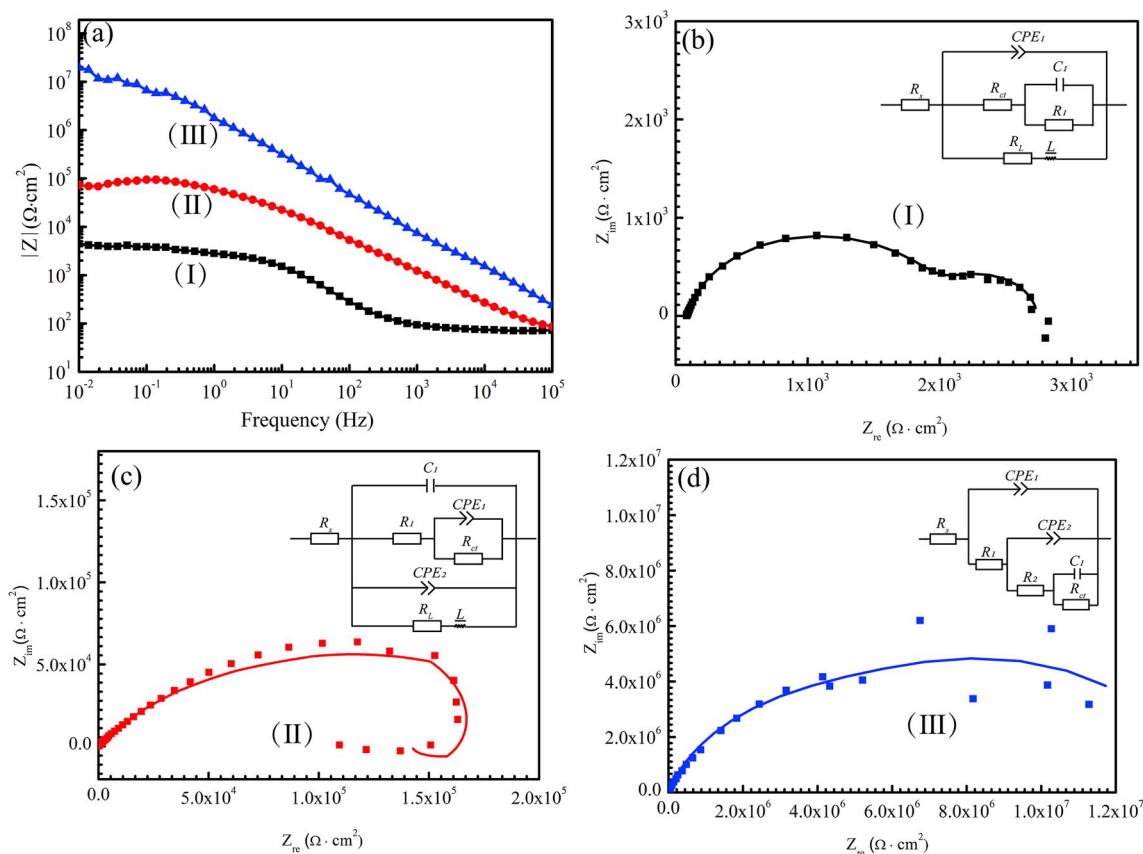
Fig. 5. (a) Bode plots and (b–d) Nyquist curves and corresponding equivalent circuits of (I) substrate, (II) MAO coating and (III) MAO/Ta$_2$O$_5$ coating immersed in Hank's solution.

E_{corr} increased from -1.70 V/SCE for MAO coating to -1.44 V/SCE for MAO/Ta$_2$O$_5$ coating, suggesting a decline in the tendency of corrosion initiation owing to thermodynamics [35,42]. That is, MAO coated samples by the ALD treatment significantly reduced the presence of micropores and microcracks in MAO coating, making the coating flatter and blocking the entry of aggressive ions into the substrate through micropores and microcracks.

Bode plots of (I) substrate, (II) MAO coating and (III) MAO/Ta$_2$O$_5$ coating immersed in Hank's solution are shown in Fig. 5a. The higher the impedance modulus are $|Z|$, at lower frequencies, the better corrosion resistance of the samples gets. The order of $|Z|$ values could be ranged in increasing order: substrate < MAO coating < MAO/Ta$_2$O$_5$ coating. Moreover, the $|Z|$ of MAO/Ta$_2$O$_5$ coating increased three orders of magnitude than that of the substrate, and two orders of magnitude than that of the MAO coating. These results disclosed that MAO coating modified through the ALD deposition of Ta$_2$O$_5$ film had a good corrosion resistance and provided better protection for the substrate. And Nyquist curves of (I) substrate, (II) MAO coating, and (III) MAO/Ta$_2$O$_5$ coating are illustrated in Fig. 5b–d. The greater the radius of curvature is, the better the corrosion resistance of the samples gets. As we can see, the MAO/Ta$_2$O$_5$ coating had the largest radius of curvature, meaning the best corrosion resistance.

The corresponding equivalent circuits of (I) substrate, (II) MAO coating and (III) MAO/Ta$_2$O$_5$ coating are displayed in Fig. 5b–d, in order to further understand the corrosion resistance of the samples. And the corresponding fitting data are listed in Table 2. R_s represents the solution resistance. R and C imply the resistance and capacitance of the corresponding coating, respectively. R_{ct} symbolizes charge transfer resistance. CPE means constant phase component. Obviously, for the substrate, the high-frequency region was composed of a constant phase component (CPE_1) and a charge transfer resistance (R_{ct}) corresponding

Table 2
Electrochemical data obtained via equivalent circuit fitting of EIS curves.

Samples	substrate	MAO coating	MAO/Ta$_2$O$_5$ coating
R_s ($\Omega \cdot cm^2$)	82.98	59.57	54.93
R_1 ($\Omega \cdot cm^2$)	2.13×10^3	1.79×10^3	3.48×10^3
R_2 ($\Omega \cdot cm^2$)	–	–	1.09×10^7
R_L ($\Omega \cdot cm^2$)	79.19	2.52×10^4	–
R_{ct} ($\Omega \cdot cm^2$)	6.09×10^2	1.23×10^5	3.99×10^6
CPE_1 ($\Omega^{-1} \cdot s^n \cdot cm^{-2}$)	1.45×10^{-5}	4.42×10^{-6}	1.81×10^{-8}
CPE_2 ($\Omega^{-1} \cdot s^n \cdot cm^{-2}$)		2.46×10^{-5}	9.08×10^{-8}
C_1 (F·cm^{-2})	9.34×10^{-4}	1.49×10^{-7}	7.22×10^{-7}
n_1	0.84	0.62	0.93
n_2	–	0.52	0.78
Chi squared	7.56×10^{-4}	4.45×10^{-3}	6.69×10^{-3}

to the electrical double layer at the interface of the substrate surface and solution. And the middle-frequency region consisting of C_1 and R_1 represented the oxidation layer formed in the air [43,44]. The low-frequency region consisted of the inductance (L) and resistance (R_L), meaning pitting of substrate and peeling of the corrosion product film [35]. For the MAO coating, the constant phase elements (C_1) and resistance (R_1) represented the porous outer layer, and the capacitance (CPE_1) and charge transfer resistance (R_{ct}) represented a dense inner layer [10]. Unfortunately, in the low-frequency region, the presence of inductance (L) meant that pitting occurred. The MAO/Ta$_2$O$_5$ coating consisted of R_1 (Ta$_2$O$_5$ film), R_2 (MAO coating) and R_{ct} (charge transfer resistance). In addition, the larger R_{ct} means better corrosion resistance of the samples. In Table 2, the value of R_{ct} ranged in the order: substrate < MAO coating < MAO/Ta$_2$O$_5$ coating. That is, the MAO/Ta$_2$O$_5$ coating had the best corrosion resistance.
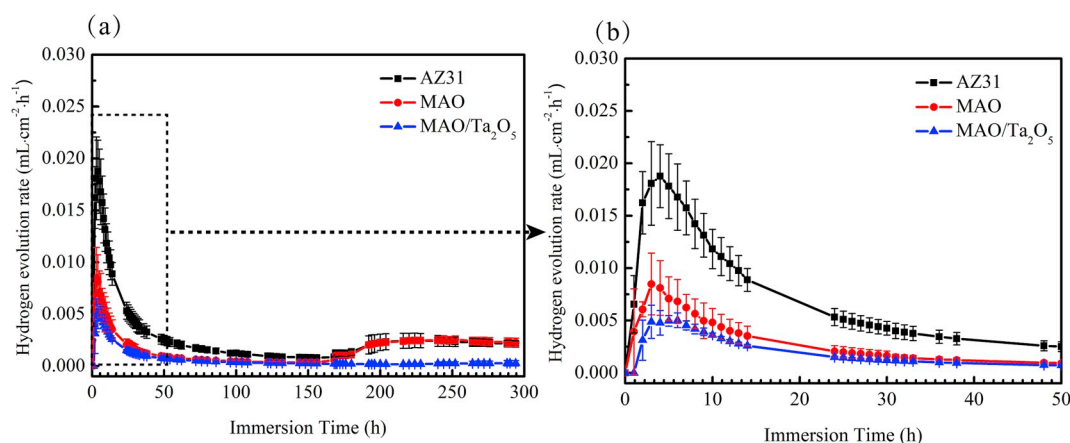
Fig. 6. (a) HER curves and (b) partial enlargement HER images of substrate, MAO coating and MAO/Ta$_2$O$_5$ coating immersed in Hank's solution for 294 h.

3.3. Immersion tests

The hydrogen evolution experiment is to further evaluate the corrosion resistance of the samples under long-term immersion. And the (a) hydrogen evolution rate (HER) curves and (b) partial enlargement HER image of substrate, MAO coating and MAO/Ta$_2$O$_5$ coating immersed in Hank's solution for 294 h are demonstrated in Fig. 6.

According to the changes of HER, it could be divided into three stages. In the first stage (0–5 h), the HERs of all samples raised rapidly to a peak due to the large amount of gas generated from the corrosion of α-Mg. For MAO and MAO/Ta$_2$O$_5$ coatings, corrosive media would penetrate the substrate through coating defects. In the second stage (5–168 h), HERs of all samples rapidly decreased and reached equilibrium, which was ascribed that corrosion products were deposited onto the exposed substrate. In the third stage (168–294 h), the HERs of the substrate and MAO coating increased, then tended to be stable, which was attributed that the corrosion product film was destroyed. Conversely, the HER of MAO/Ta$_2$O$_5$ coating was essentially unchanged, indicating that the MAO coating modified by ALD treatment had a better corrosion resistance.

3.4. Corrosion morphologies analysis

Macro-morphologies of (a) substrate, (b) MAO coating and (c) MAO/Ta$_2$O$_5$ coating immersed in Hank's solution for 294 h are shown in Fig. 7. As shown in Fig. 7a, AZ31 substrate was corroded, especially near the edge region with a deep etch pit, indicating that the corrosion was very serious. For the MAO coating in Fig. 7b, a large number of etch pits were found near the edges of the sample and the pre-punched locations. Note that, most areas of the MAO/Ta$_2$O$_5$ coating were intact after long-term soaking and the traces on the sample surface were mostly scratches formed when the sample was stored later. Thus, the corrosion resistance of the sample treated through the ALD technique was effectively improved, which was consistent with the corrosion rate in Fig. 6.
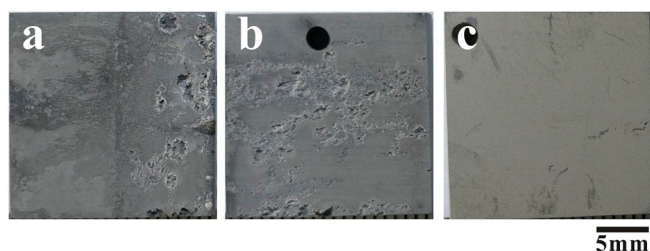

Fig. 7. Macro-morphologies of (a) substrate, (b) MAO coating and (c) MAO/Ta$_2$O$_5$ coating immersed in Hank's solution for 294 h.

Fig. 8 illustrates SEM images of (a) substrate, (b) MAO coating and (c, d) MAO/Ta$_2$O$_5$ coating immersed in Hank's solution for 294 h. A large number of cracks were observed on the substrate surface in Fig. 8a. The MAO coating also had a large number of cracks, and the structure of the micropores became smaller, which might be micropores were blocked through the corrosion products (Fig. 8b). However, the original microcracks in MAO coating expanded into large cracks after soaking, which could be ascribed that the aggressive ions invaded the substrate along micropores and microcracks, producing a large amount of hydrogen to cause cracking of the coating and accelerate corrosion. In addition, the MAO/Ta$_2$O$_5$ coating was relatively complete in Fig. 8c. However, pits were found in some areas of the MAO/Ta$_2$O$_5$ coating (Fig. 8d), which meant the initiation of pitting corrosion, and then corrosion would propagate around the pits as immersion time. Furthermore, according to our previous research [8,12], pitting might be located near the intermetallic compound Al–Mn phase.

EDS mappings are shown in Fig. 9 for (a) substrate, (b) MAO coating and (c, d) MAO/Ta$_2$O$_5$ coating immersed in Hank's solution for 294 h. For the substrate and MAO coating, the corroded samples mainly contained Mg, O, P and Ca elements. And the presence of P and Ca elements meant the deposition of corrosion products (Ca–P products). Conversely, the MAO/Ta$_2$O$_5$ coating mainly contained Mg, O, P and Ta elements, and the Ta element was still uniformly distributed. The Ca element was not detected, indicating that there was no deposition of corrosion products on the surface. Also, the pitting area of MAO/Ta$_2$O$_5$ coating contained some P, O and Ca elements, as well as fewer Mg elements, which indicated that the corrosion products were deposited in the corroded area. Although not Al or Mn elements were detected, pitting might occur near the second phase (*i.e.* Al–Mn phase) in the Mg alloy AZ31 according to our previous research [8,12].

4. Discussion

4.1. Comparison of corrosion resistance

Fig. 10a shows the different cycles time (*i.e.* different thicknesses) of Ta$_2$O$_5$ film on MAO coating of (I) 500- and (II) 1000-cycles. The thickness of the 500-cycles Ta$_2$O$_5$ film was approximately 50 nm, which corresponding i_{corr} was 2.23×10^{-9} A/cm^2. The thickness of the 1000-cycles Ta$_2$O$_5$ was approximately 100 nm, and the corresponding i_{corr} was decreased 50% and reached 1.06×10^{-9} A/cm^2. Obviously, as increasing times of cycles, the thickness of the Ta$_2$O$_5$ film increased and i_{corr} decreased. That is, the corrosion resistance of Ta$_2$O$_5$ film was enhanced significantly with thickness.

Fig. 10b demonstrates a comparison of the corrosion resistance of several composite coatings based on MAO coated substrate. Cui et al. [35] constructed a PMTMS coating on the surface of MAO coated Mg
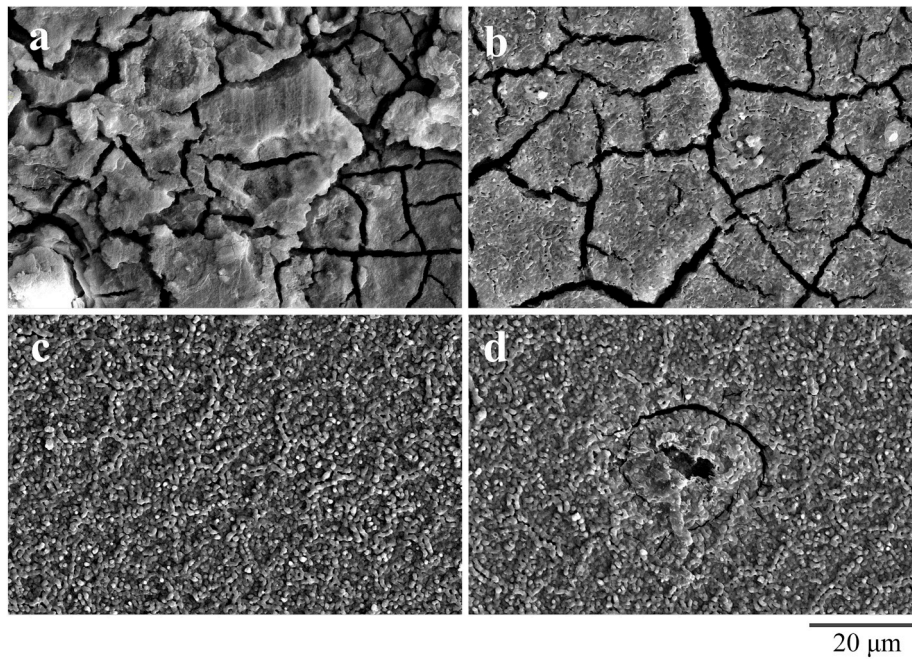
Fig. 8. SEM images of (a) substrate, (b) MAO coating and (c, d) MAO/Ta$_2$O$_5$ coating immersed in Hank's solution for 294 h.
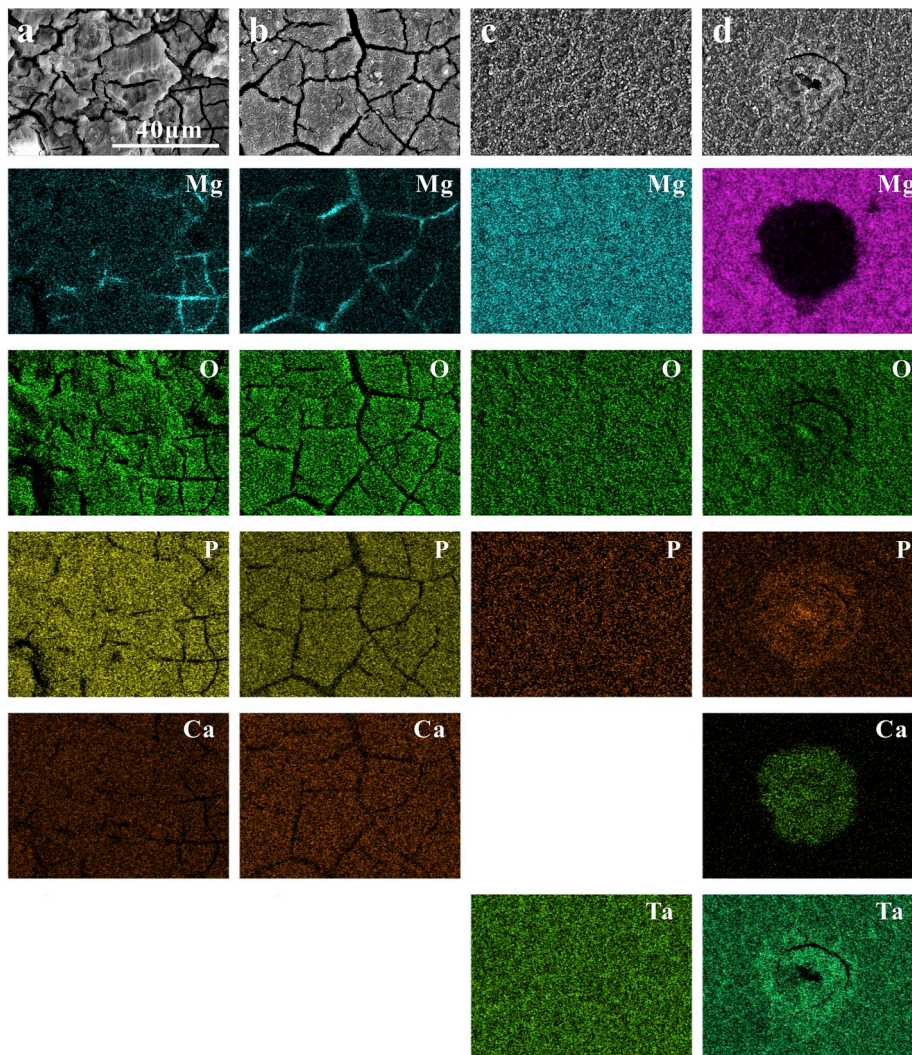

Fig. 9. SEM images and EDS mappings of (a) substrate, (b) MAO coating and (c, d) MAO/Ta$_2$O$_5$ coating immersed in Hank's solution for 294 h.
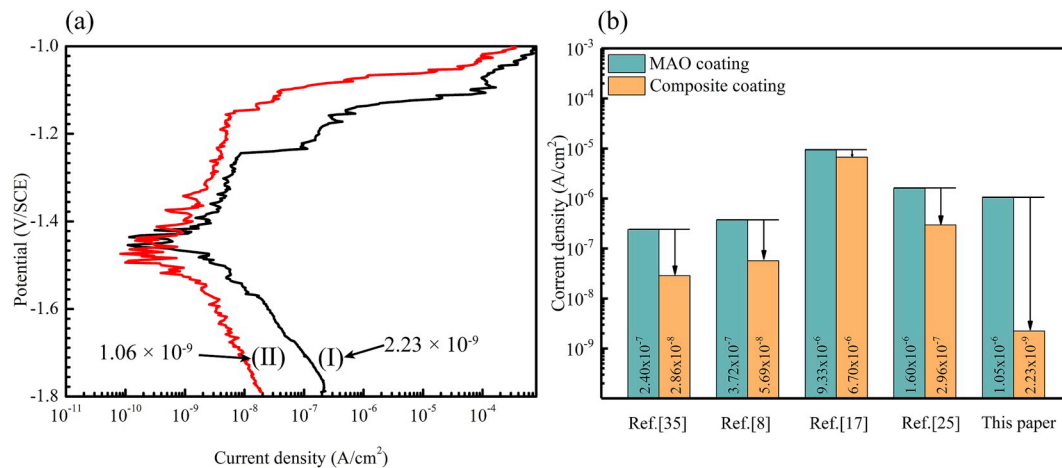
Fig. 10. (a) Different cycles time of Ta_2O_5 film on MAO coating of (I) 500- and (II) 1000-cycles; (b) a comparison of the corrosion resistance of several composite coatings based on MAO coated substrates.
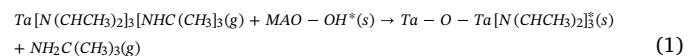
alloy AZ31. The i_{corr} was reduced from 2.40×10^{-7} A/cm^2 for the MAO coating to 2.86×10^{-8} A/cm^2 for the MAO/PMTMS composite coating. Li et al. [8] prepared a $Mg(OH)_2$ coating on the surface of MAO coated Mg alloy AZ31 by in situ growth method, and the corresponding i_{corr} decreased from 3.72×10^{-7} A/cm^2 to 5.69×10^{-8} A/cm^2. Chitosan coating was prepared on the surface of MAO coated Mg–1Li–1Ca by Yu et al. [17], and its corrosion resistance was limited. Zeng et al. [25] prepared a PLA coating on the surface of MAO coated Mg–1Li–1Ca, which the i_{corr} of the MAO/PLA composite coating decreased one order of magnitude lower than that of the MAO coating. The above composite coatings were all organic coatings, and the risk of organic coatings being easily hydrolyzed and detached might cause coating failure, which in turn led to a decrease in corrosion resistance. In this study, the i_{corr} of the MAO/Ta_2O_5 coating decreased three orders of magnitude than that of the MAO coating, greatly improving corrosion resistance. The results revealed that Ta_2O_5 film with dense and smooth and good corrosion resistance was prepared on the surface of MAO coating based on the advantages (self-limiting and self-saturating method) of ALD technology and the excellent corrosion resistance of Ta metal.

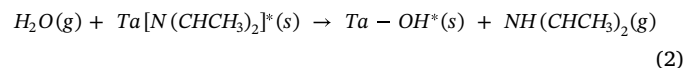### 4.2. Formation mechanism of MAO/Ta_2O_5 coating

ALD technology is a self-limiting and self-saturating method to form a thin film through alternately introducing a gas precursor pulse into the reaction chamber and occurring a surface chemical reaction on the substrate surface. Obviously, the deposition of Ta_2O_5 using ALD is a discontinuous process consisting of several semi-reactive sequences. Taking $Ta[N(CHCH_3)_2]_3[NHC(CH_3)_3]$ as Ta source and water vapor as O source, the whole reaction could be divided into two steps in Fig. 11a. The first step (Reaction 1), $Ta[N(CHCH_3)_2]_3[NHC(CH_3)_3]$ was introduced into the reaction chamber in the form of a gas. Then, a reaction occurred on MAO coating surface (a large number of –OH active sites on MAO coating surface) to rob the H of MAO-OH* (* representing a functional group adsorbed on the deposition surface) and form the intermediate layer Ta–O–Ta[N(CHCH$_3$)$_2$]$_3$*. And a by-product $NH_2C(CH_3)_3$ was formed in this process. After the reaction was completed, the remaining Ta source and reaction by-products were purged bypassing high-purity nitrogen [45,46]. The second step (Reaction 2), an excess of O source (i.e. water vapor) was introduced to react with the reactive site –N(CHCH$_3$)$_2$ of the intermediate layer to obtain a layer of Ta_2O_5 and reaction by-products [47]. Due to the steric hindrance effect, the O source would first react with –NHC(CH$_3$)$_3$ and then replaced the –N(CHCH$_3$)$_2$ groups. After the residual gas was purged with high purity nitrogen, one cycle ended. A Ta_2O_5 film was obtained in each cycle, and

each of the half-reacted precursors could be adsorbed inside the micropores and microcracks of MAO coating. Finally, a dense Ta_2O_5 coating was obtained after a plurality of cycles of deposition (Fig. 11b).
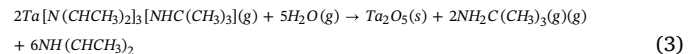
Reaction 1

$$Ta[N(CHCH_3)_2]_3[NHC(CH_3)_3](g) + MAO-OH^*(s) \rightarrow Ta-O-Ta[N(CHCH_3)_2]_3^*(s)$$
$$+ NH_2C(CH_3)_3(g) \tag{1}$$

Reaction 2:

$$H_2O(g) + Ta[N(CHCH_3)_2]^*(s) \rightarrow Ta-OH^*(s) + NH(CHCH_3)_2(g) \tag{2}$$

And Fig. 11c demonstrates the reaction of Ta_2O_5 as follows:

$$2Ta[N(CHCH_3)_2]_3[NHC(CH_3)_3](g) + 5H_2O(g) \rightarrow Ta_2O_5(s) + 2NH_2C(CH_3)_3(g)(g)$$
$$+ 6NH(CHCH_3)_2 \tag{3}$$

4.3. The corrosion resistance mechanism of MAO/Ta_2O_5 coating

The MAO coated sample treated by ALD deposition of Ta_2O_5 was more complete than the substrate and the single MAO coating. This was mainly because ALD technology was used to prepare nano-scale film based on two continuous and periodic self-limiting half-reactions. And the dense Ta_2O_5 could well seal microcracks and through holes. The Ta_2O_5 film acted as a physical barrier in the corrosive medium and could effectively block the entry of aggressive ions, thereby effectively protecting the substrate from corrosion during the immersion test. Through the PDP curves, EIS plots and immersion test, it could be clearly found that the MAO/Ta_2O_5 coating had good corrosion resistance. However, there were still some nano-gaps during the deposition process. As the immersion time increased, the aggressive ions would penetrate the Ta_2O_5 nano-layer through these gaps. Therefore, the hydrogen produced through the chemical reaction between H_2O and α-Mg would eventually lead to local damage of the Ta_2O_5 nanofilm, causing the pitting corrosion (as shown in Fig. 12).

5. Conclusions

(1) The Ta_2O_5 nanofilm deposited on MAO coating by ALD technology effectively sealed the micropores and microcracks in MAO coating, and the film was evenly distributed without obvious defects.
(2) Ta_2O_5 nanofilm was mainly present in the form of amorphousness.
(3) Electrochemical test results showed that the i_{corr} of MAO/Ta_2O_5 coating decreased three orders of magnitude than that of the substrate and MAO coating. Conversely, due to the porous and microcracked structure of the MAO coating, the improvement in corrosion resistance was limited. The hydrogen evolution
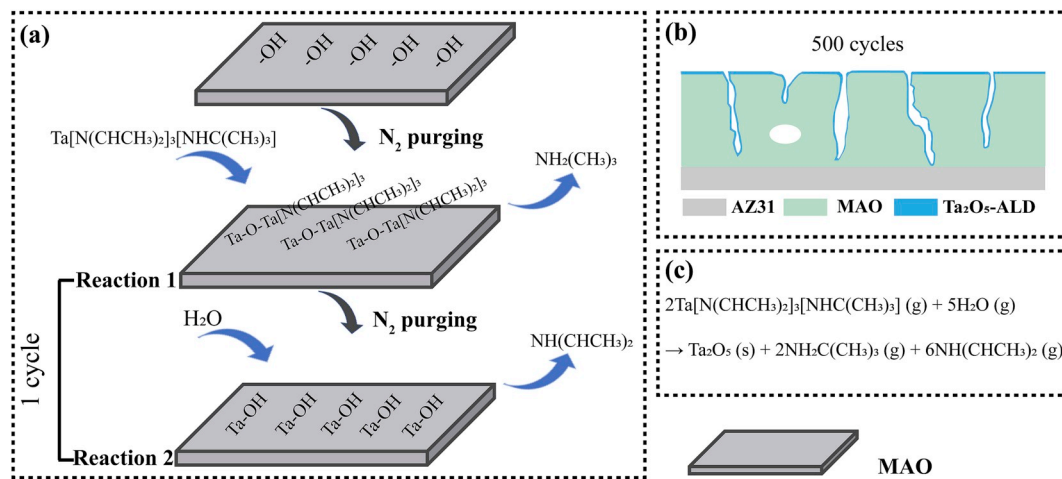
Fig. 11. Schematic illustration of MAO/Ta$_2$O$_5$ coating through ALD for (a) 1 and (b) 500 cycles and (c) the reaction equation of Ta$_2$O$_5$.
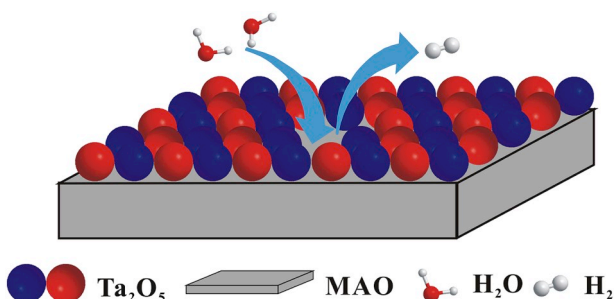

Fig. 12. Schematic illustration of the corrosion resistance mechanism of the MAO/Ta$_2$O$_5$ coating.

experiments also revealed that the MAO/Ta$_2$O$_5$ coating had the best corrosion resistance.

(4) Pitting corrosion occurred on the MAO/Ta$_2$O$_5$ coating. And the corrosion initiated near the intermetallic compound Al–Mn particles and then gradually expanded outward.

Author contribution

Chang-Yang Li: Data Curation, Writing - original draft, Chi Yu: Methodology, Investigation, Data Curation, Writing - original draft, Rong-Chang Zeng: Conceptualization, Funding acquisition, Writing - review & editing, Bo-Cheng Zhang: Conceptualization, Resources, Writing - review & editing. Lan-Yue Cui: Writing - review & editing. Jun Wan: Resources, Yang Xia: Supervision.

Declaration of competing interest

None.

Acknowledgements

References

[1] L.Y. Li, L.Y. Cui, R.C. Zeng, S.Q. Li, X.B. Chen, Y. Zheng, M.B. Kannan, Advances in functionalized polymer coatings on biodegradable magnesium alloys-A review, Acta Biomater. 79 (2018) 23–36.

[2] X.B. Yu, W. Huang, D.W. Zhao, K. Yang, L.L. Tan, X.Z. Zhang, J.L. Li, M. Zhang, S. Zhang, T. Liu, B.L. Wu, M.J. Qu, R.M. Duan, Y.S. Yuan, Study of engineered low-modulus Mg/PLLA composites as potential orthopaedic implants: an in vitro and in vivo study, Colloids Surf., B 174 (2019) 280–290.

[3] Y.H. Zou, J. Wang, L.Y. Cui, R.C. Zeng, Q.Z. Wang, Q.X. Han, J. Qiu, X.B. Chen, D.C. Chen, S.K. Guan, Y.F. Zheng, Corrosion resistance and antibacterial activity of zinc-loaded montmorillonite coatings on biodegradable magnesium alloy AZ31, Acta Biomater. 98 (2019) 196–214, https://doi.org/10.1016/j.actbio.2019.1005.1069.

[4] J.L. Wang, F. Witte, T.F. Xi, Y.F. Zheng, K. Yang, Y.S. Yang, D.W. Zhao, J. Meng, Y.D. Li, W.R. Li, K.M. Chan, L. Qin, Recommendation for modifying current cyto-toxicity testing standards for biodegradable magnesium-based materials, Acta Biomater. 21 (2015) 237–249.

[5] L.D. Hou, Z. Li, Y. Pan, M. Sabir, Y.F. Zheng, L. Li, A review on biodegradable materials for cardiovascular stent application, Front. Mater. Sci. 10 (2016) 238–259.

[6] D.D. Xia, Y. Liu, S.Y. Wang, R.C. Zeng, Y.S. Liu, Y.F. Zheng, Y.S. Zhou, In vitro and in vivo investigation on biodegradable Mg-Li-Ca alloys for bone implant applica-tion, Sci. China Mater. 62 (2019) 256–272.

[7] L.Y. Li, L.Y. Cui, B. Liu, R.C. Zeng, X.B. Chen, S.Q. Li, Z.L. Wang, E.H. Han, Corrosion resistance of glucose-induced hydrothermal calcium phosphate coating on pure magnesium, Appl. Surf. Sci. 465 (2019) 1066–1077.

[8] C.Y. Li, X.L. Fan, R.C. Zeng, L.Y. Cui, S.Q. Li, F. Zhang, Q.K. He, M.B. Kannan, H.W. Jiang, D.C. Chen, S.K. Guan, Corrosion resistance of in-situ growth of nano-sized Mg(OH)$_2$ on micro-arc oxidized magnesium alloy AZ31-Influence of EDTA, J. Mater. Sci. Technol. 35 (2019) 1088–1098.

[9] Y.S. Feng, X. Ma, L. Chang, S.J. Zhu, S.K. Guan, Characterization and cyto-compatibility of polydopamine on MAO-HA coating supported on Mg-Zn-Ca alloy, Surf. Interface Anal. 49 (2017) 1115–1123.

[10] C.Y. Li, X.L. Feng, X.L. Fan, X.T. Yu, Z.Z. Yin, M.B. Kannan, X.B. Chen, S.K. Guan, J. Zhang, R.C. Zeng, Corrosion and wear resistance of micro-arc oxidation com-posite coatings on magnesium alloy AZ31-The influence of inclusions of carbon spheres, Adv. Eng. Mater. 21 (2019) 1–16.

[11] W. Peng, J.X. Chen, X.F. Shan, Y.C. Wang, F. He, X.J. Wang, L.L. Tan, K. Yang, Mg-based absorbable membrane for guided bone regeneration (GBR): a pilot study, Rare Met. 38 (2019) 577–587.

[12] X.L. Fan, Y.F. Huo, C.Y. Li, M.B. Kannan, X.B. Chen, S.K. Guan, R.C. Zeng, Q.L. Ma, Corrosion resistance of nanostructured magnesium hydroxide coating on magne-sium alloy AZ31: influence of EDTA, Rare Met. 38 (2019) 520–531.

[13] L.Y. Cui, G.B. Wei, R.C. Zeng, S.Q. Li, Y.H. Zou, E.H. Han, Corrosion resistance of a novel SnO$_2$ -doped dicalcium phosphate coating on AZ31 magnesium alloy, Bioact. Mater. 3 (2017) 245–249.

[14] L. Chen, J.A. Li, J.W. Chang, S.B. Jin, D. Wu, H.H. Yan, X.F. Wang, S.K. Guan, Mg-Zn-Y-Nd coated with citric acid and dopamine by layer-by-layer self-assembly to improve surface biocompatibility, Sci. China Technol. Sci. 61 (2018) 1228–1237.

[15] X.J. Ji, L. Gao, J.C. Liu, J. Wang, Q. Cheng, J.P. Li, S.Q. Li, K.Q. Zhi, R.C. Zeng, Z.L. Wang, Corrosion resistance and antibacterial properties of hydroxyapatite coating induced by gentamicin-loaded polymeric multilayers on magnesium alloys, Colloids Surf., B 179 (2019) 429–436.

[16] W. Yuan, B. Li, D.F. Chen, D.H. Zhu, Y. Han, Y.F. Zheng, Formation mechanism, corrosion behavior, and cytocompatibility of microarc oxidation coating on ab-sorbable high-purity zinc, ACS Biomater. Sci. Eng. 5 (2018) 487–497.

[17] C. Yu, L.Y. Cui, Y.F. Zhou, Z.Z. Han, X.B. Chen, R.C. Zeng, Y.H. Zou, S.Q. Li, F. Zhang, E.H. Han, S.K. Guan, Self-degradation of micro-arc oxidation/chitosan composite coating on Mg-4Li-1Ca alloy, Surf. Coat. Technol. 344 (2018) 1–11.

[18] M.B. Sedelnikova, E.G. Komarova, Y.P. Sharkeev, T.V. Tolkacheva, I.A. Khlusov, L.S. Litvinova, K.A. Yurova, V.V. Shupletsova, Comparative investigations of structure and properties of micro-arc wollastonite-calcium phosphate coatings on titanium and zirconium-niobium alloy, Bioact. Mater. 2 (2017) 177–184.

[19] M.B. Kannan, R. Walter, A. Yamamoto, H. Khakbaz, C. Blawert, Electrochemical surface engineering of magnesium metal by plasma electrolytic oxidation and

calcium phosphate deposition: biocompatibility and in vitro degradation studies, RSC Adv. 8 (2018) 29189–29200.

[20] L.Y. Cui, R.C. Zeng, S.K. Guan, W.C. Qi, F. Zhang, S.Q. Li, E.H. Han, Degradation mechanism of micro-arc oxidation coatings on biodegradable Mg-Ca alloys: the influence of porosity, J. Alloy. Comp. 695 (2017) 2464–2476.

[21] Z.C. Wang, X.J. Tang Yi, Study on the micro-arc oxidation and surface treatment of AZ91D magnesium alloy, J. Xiamen Univ., Nat. Sci. 45 (2006) 292–295.

[22] Seong Jong Kim, Jeong Il Kim, M. Okido, Sealing effects of anodic oxide films formed on Mg-Al alloys, Korean J. Chem. Eng. 21 (2004) 915–920.

[23] D.Y. Shan, R.F. Zhang, E.H. Han, Effect of Al_2O_3 thin film on corrosion resistance of pure Mg and its anodic coating, Mater. Sci. Forum 488–489 (2005) 865–868.

[24] Q.Z. Cai, D. Wang, H.H. Luo, B.K. Wei, Sealing of micro-arc oxidation coating on magnesium alloy by SiO_2 sol sealing agent, Special Cast. Nonferrous Alloys 26 (2006) 612–614.

[25] R.C. Zeng, L.Y. Cui, K. Jiang, R. Liu, B.D. Zhao, Y.F. Zheng, In vitro corrosion and cytocompatibility of a microarc oxidation coating and poly(L-lactic acid) composite coating on Mg-1Li-1Ca alloy for orthopedic implants, ACS Appl. Mater. Interfaces 8 (2016) 10014–10028.

[26] V. Miikkulainen, M. Leskelä, M. Ritala, R.L. Puurunen, Crystallinity of inorganic films grown by atomic layer deposition: overview and general trends, J. Appl. Phys. 113 (2013) 021301-021301-021301-021101.

[27] R.W. Johnson, A. Hultqvist, S.F. Bent, A brief review of atomic layer deposition: from fundamentals to applications, Mater. Today 17 (2014) 236–246.

[28] J.C. Deng, Y. Wang, The metal tantalum in orthopedic applications, J. Biomed. Eng. 28 (2011) 420–422.

[29] H. Wang, K.X. Su, L.Z. Su, P.P. Liang, P. Ji, C. Wang, Comparison of 3D-printed porous tantalum and titanium scaffolds on osteointegration and osteogenesis, Mater. Sci. Eng. C Mater. Biol. Appl. 104 (2019) 109908.

[30] A. Rodriguez Contreras, J. Guillem Marti, O. Lopez, J.M. Manero, E. Ruperez, Antimicrobial PHAs coatings for solid and porous tantalum implants, Colloids Surfaces B Biointerfaces 182 (2019) 110317.

[31] J. Lu, X.P. Zheng, Z.Q. Wang, Application of porous tantalum implant in treatment of bone defect, Chin. J. Reparative Reconstr. Surg. 26 (2012) 244–247.

[32] J. Xu, X.K. Bao, T. Fu, Y.H. Lyu, P. Munroe, Z.H. Xie, In vitro biocompatibility of a nanocrystalline β-Ta_2O_5 coating for orthopaedic implants, Ceram. Int. 44 (2018) 4660–4675.

[33] L.D. Salmi, E. Puukilainen, M. Vehkamäki, M. Heikkilä, M. Ritala, Atomic layer deposition of Ta_2O_5/polyimide nanolaminates, Chem. Vap. Depos. 15 (2009) 221–226.

[34] M. Kim, W. Kim, T. Lee, H. Kim, Growth characteristics and electrical properties of Ta_2O_5 grown by thermal and O_3-based atomic layer deposition on TiN substrates for metal-insulator-metal capacitor applications, Thin Solid Films 542 (2013) 71–75.

[35] L.Y. Cui, S.D. Gao, P.P. Li, R.C. Zeng, F. Zhang, S.Q. Li, E.H. Han, Corrosion resistance of a self-healing micro-arc oxidation/polymethyltrimethoxysilane composite coating on magnesium alloy AZ31, Corros. Sci. 118 (2017) 84–95.

[36] A. Jara, B. Fraisse, V. Flaud, N. Fréty, G. Gonzalez, Thin film deposition of Ta, TaN and Ta/TaN bi-layer on Ti and SS316-LVM substrates by RF sputtering, Surf. Coat. Technol. 309 (2017) 887–896.

[37] K.V. Egorov, Y.Y. Lebedinskii, A.M. Markeev, O.M. Orlov, Full ALD Ta_2O_5-based stacks for resistive random access memory grown with in vacuo XPS monitoring, Appl. Surf. Sci. 356 (2015) 454–459.

[38] Y.Z. Fan, X. Cheng, Porous IrO_2-Ta_2O_5 coating modified with carbon nanotubes for oxygen evolution reaction, J. Electrochem. Soc. 163 (2016) E209–E215.

[39] F. Volpi, L. Cadix, G. Berthomé, E. Blanquet, N. Jourdan, J. Torres, XPS studies of the ALD-growth of TaN diffusion barriers: impact of the dielectric surface chemistry on the growth mechanism, Microelectron. Eng. 85 (2008) 2068–2070.

[40] J.C. Woo, C.I. Kim, Dry etching of TaN thin film using CH_4/Ar inductively coupled plasma, Vacuum 86 (2011) 1–6.

[41] M. Mehdipour, S.H. Tabaian, S. Firoozi, Effect of IrO_2 crystallinity on electro-catalytic behavior of IrO_2-Ta_2O_5/MWCNT composite as anodes in chlor-alkali membrane cell, Ceram. Int. 45 (2019) 19971–19980.

[42] L.Y. Cui, H.P. Liu, W.L. Zhang, Z.Z. Han, M.X. Deng, R.C. Zeng, S.Q. Li, Z.L. Wang, Corrosion resistance of a superhydrophobic micro-arc oxidation coating on Mg-4Li-1Ca alloy, J. Mater. Sci. Technol. 33 (2017) 1263–1271.

[43] Z.Y. Ding, L.Y. Cui, X.B. Chen, R.C. Zeng, S.K. Guan, S.Q. Li, F. Zhang, Y.H. Zou, Q.Y. Liu, In vitro corrosion of micro-arc oxidation coating on Mg-1Li-1Ca alloy-The influence of intermetallic compound Mg_2Ca, J. Alloy. Comp. 764 (2018) 250–260.

[44] Y. Wang, B.H. Ding, S.Y. Gao, X.B. Chen, R.C. Zeng, L.Y. Cui, S.J. Li, S.Q. Li, Y.H. Zou, E.H. Han, S.K. Guan, Q.Y. Liu, In vitro corrosion of pure Mg in phosphate buffer solution-Influences of isoelectric point and molecular structure of amino acids, Mater. Sci. Eng. C Mater. Biol. Appl. 105 (2019) 110042.

[45] X.M. Liu, Q.Y. Yang, Z.Y. Li, W. Yuan, Y.F. Zheng, Z.D. Cui, X.J. Yang, K.W.K. Yeung, S.L. Wu, A combined coating strategy based on atomic layer deposition for enhancement of corrosion resistance of AZ31 magnesium alloy, Appl. Surf. Sci. 434 (2018) 1101–1111.

[46] M.L. Chang, L.C. Wang, H.C. Lin, M.J. Chen, K.M. Lin, Investigation of defects in ultra-thin Al_2O_3 films deposited on pure copper by the atomic layer deposition technique, Appl. Surf. Sci. 359 (2015) 533–542.

[47] Q.Y. Yang, W. Yuan, X.M. Liu, Y.F. Zheng, Z.D. Cui, X.J. Yang, H.B. Pan, S.L. Wu, Atomic layer deposited ZrO_2 nanofilm on Mg-Sr alloy for enhanced corrosion resistance and biocompatibility, Acta Biomater. 58 (2017) 515–526.